

# Evolution of galaxy dynamics over the last 10 Gyrs with MUSE/VLT

Master Thesis



**Author:** Mercier Wilfried

**Supervisor:** Contini Thierry

**Co-Supervisor:** Epinat Benoît

Observatoire de Paris

Institut de Recherche en Astronomie et Planétologie

Laboratoire d'Astrophysique de Marseille

June 11, 2019





# Abstract

# Contents

<b>1</b>	<b>Introduction</b>	<b>1</b>
1.1	Current topics in galactic astronomy . . . . .	1
1.1.1	A global picture of the Universe . . . . .	1
1.2	What we have learned about galaxies so far . . . . .	2
1.2.1	Evolving properties with redshift ? . . . . .	2
1.2.2	An impact from the environment ? . . . . .	3
1.3	Observation techniques in astronomy . . . . .	4
1.3.1	Spectroscopy and photometry . . . . .	4
1.3.2	Long slit and early integral field spectroscopy . . . . .	6
<b>2</b>	<b>Sample selection</b>	<b>8</b>
2.1	MUSE-GTO MAGIC . . . . .	8
2.2	COSMOS field . . . . .	8
2.3	Prior information on the galaxies . . . . .	9
2.3.1	Galaxies in structures . . . . .	9
2.3.2	Morphological information from COSMOS catalogues . . . . .	10
2.4	Checking catalogues values consistency . . . . .	11
2.4.1	Reasons for checking catalogues values . . . . .	11
2.4.2	Catalogues used for comparison . . . . .	12
2.4.3	Total magnitudes . . . . .	12
2.4.4	Morphological type classification . . . . .	14
2.4.5	Half-light radii . . . . .	17
2.4.6	Ellipticity . . . . .	19
2.5	SNR and size selection . . . . .	20
2.5.1	Size selection . . . . .	20
2.5.2	SNR selection . . . . .	21
2.6	Characterisation of the sample . . . . .	22
2.6.1	Selecting galaxies . . . . .	22
2.6.2	Redshift distribution . . . . .	23
2.6.3	Mass-SFR relation . . . . .	24
<b>3</b>	<b>Kinematical modelling</b>	<b>26</b>
3.1	Manual cleaning . . . . .	26
3.2	Kinematical parametrisation . . . . .	26
3.3	Model . . . . .	27
3.4	Maximum velocity and velocity dispersion . . . . .	28
	<b>References</b>	<b>29</b>

<b>A</b>	<b>Details about morphological classification</b>	<b>34</b>
A.1	Non-parametric values . . . . .	34
A.1.1	Concentration . . . . .	34
A.1.2	Asymmetry . . . . .	35
A.1.3	Gini coefficient . . . . .	35
<b>B</b>	<b>PSF FWHM variation with wavelength and MUSE field</b>	<b>36</b>

## List of Figures

1	Error on inclination as a function of $b/a$ and its error. . . . .	11
2	Comparison between magnitudes . . . . .	13
3	Morphological types comparison . . . . .	14
4	Radii comparison between catalogues and GALFIT using bulb and disk . .	16
5	Radii comparison per catalogue . . . . .	16
6	Bias before/after correction . . . . .	18
7	Ellipticity comparison . . . . .	19
8	Selected sample . . . . .	20
9	Redshift distribution . . . . .	22
10	SFR-mass relation . . . . .	24
11	PSF FWHM variation with wavelength. . . . .	36

## List of Tables

1	Main characteristics of the observed MUSE fields . . . . .	8
---	--	---



# 1 Introduction

## 1.1 Current topics in galactic astronomy

### 1.1.1 A global picture of the Universe

Our knowledge of galaxy properties and their evolution through time has drastically changed from the early 20th century when the Grand Debate (Shapley & Curtis, 1921) between Harlow Shapley and Heber Curtis on the (extra)galactic origin of the so-called nebulae took place (see Trimble (1995) for an interesting discussion on the subject). Since Hubble (1926), Hubble (1929) measurement of these nebulae distances to us, we know they actually are galaxies like our own lying at great distances and moving away from us. This global movement was understood in the cosmological framework of an expanding Universe. In a few months of interval, in 1998-1999, two teams measured the redshift and distance of far distant type Ia supernovae, considered as standard candles, and held evidence for an accelerating expansion which revived the need of a cosmological constant in Einstein's field equations (Riess et al., 1998), (Perlmutter et al., 1999). This additional term has been interpreted as a fluid with negative pressure acting against gravity, and is known as dark energy. Additionally, the first evidence of a dark component in galaxy clusters mass distribution was suggested by Fritz Zwicky (Zwicky, 1933), (Zwicky, 1937). By measuring the relative velocity of 7 galaxies in Coma Berenices, he derived a velocity dispersion  $\sigma_v$  from which he computed with the virial theorem an order of magnitude for the cluster dynamical mass  $M_d \sim (\sigma_v^2 R)/G$ , with  $R$  the cluster characteristic size. The given mass was roughly two orders of magnitude above the expected luminous mass from the luminosity of the galaxies. However, this argument never really convinced the other astronomers at the time. A stronger proof for the existence of a dark component embedded in galaxies came from the study of galaxy rotation curves performed by Vera Rubin in the 1970s (Rubin & Ford, 1970), (Rubin et al., 1978). By looking at the outer material of galaxies, she observed flat rotation curves which either indicated a deviation from Newton's law of gravitation or the presence of large amounts of dark matter in surrounding haloes.

From this point onward, the need of a unified cosmological model including these new aspects became obvious. Decades of observations, state of the art N-body simulations and measurements of cosmological probes have given the actual  $\Lambda$ CDM model its renown. In the meantime, as cosmology advanced and the size of the Universe exploded following Hubble 1929 publication, a new branch of astronomy centred on galaxies quickly developed both in terms of observations and of theoretical modelling.



## 1.2 What we have learned about galaxies so far

### 1.2.1 Evolving properties with redshift ?

Nowadays, galaxies are understood as gravitationally bound collections of stars, gas and dust which are supposed to have collapsed from initial clouds embedded in rapidly growing dark matter haloes. Galaxies formation and evolution should therefore follow the growth of the dark matter distribution through space and time, and as such should be tightly correlated to the global properties of our Universe.

In the local Universe, galaxies can be divided into two categories based on their shape and colour: red ellipticals and blue spirals. These are also referred to as early and late type respectively according to Hubble (1922), Hubble (1926) classification. Even though this is true for most galaxies, we also observe a small fraction of dustier red spirals. Nevertheless, the separation is clear with very few galaxies in between the two populations. Ellipticals tend to be the most massive ( $M \sim 1 - 5 \times 10^{11} M_{\odot}$ ), as well as quenched, that is their Star Formation Rate (SFR) is near 0. Most of their massive younger and bluer stars are gone (as a star's lifetime scales as its mass to the power of 3 or so) leaving only old red stars, which is the reason for their red colour. On the other hand, spirals are more recent, star-forming galaxies, still full of blue stars, but also smaller and lighter. When looking at more distant parts of the Universe, say  $z > 0.5$ , this dichotomy is less pronounced. Giant ellipticals are more rare, those found are still forming stars and disk-like galaxies have more irregular morphologies which might be due to past merger events or unrelaxed kinematics because of a recent formation.

Assigning a characteristic velocity and a velocity dispersion, which are two key parameters used virtually in every kinematical study, to a galaxy is not a straightforward step. Generally, this is done by fitting a model onto some velocity measurement which requires spectroscopic data (3D cube or slit). Almost all galaxies are found to have flat rotation curves because of their dark matter content (except perhaps for some dwarf galaxies but these are too small to be detected at high redshift). By flat, we mean that they have a steadily rising slope from the central part until it reaches a turnover point where the curve flattens, a so-called plateau, or where it slowly decreases. In this case, the characteristic velocity which is taken into account is, most of the time, the maximum velocity at the turnover, or the plateau velocity  $V_{\text{max}}$ . On the other hand, there are various ways of computing the velocity dispersion  $\sigma_v$ , but all ultimately describe the amplitude of unordered, incoherent motion within the galaxy.

In the local Universe, most spirals have low velocity dispersion compared to their rotational velocity. The opposite is true for elliptical galaxies with high velocity dispersion but no significant rotation. For more distant galaxies, this might not be true any more with

a much higher fraction of spiral or disk-like galaxies<sup>1</sup> with high velocity dispersion. Usually, the parameter  $V_{\text{max}}/\sigma_v$  is used to classify a galaxy as either rotationally supported ( $> 1$ ) or as dispersion dominated ( $< 1$ ). High redshift dispersion dominated galaxies were first discovered by (insert Erb et al 2006a paper here). These are different from the "dispersion dominated" giant ellipticals we see in the local Universe as they are less massive, more compact and yet highly star forming. Some authors hypothesized that the dispersion dominated galaxies are ancestors of the modern large ellipticals, growing by subsequent merging, or perhaps just the ancestors of the few small ellipticals we see today. Nevertheless, if there is any relation between these two populations, it is still not clear what it is. As we do not know if these dispersion dominated systems are due to unresolved rotation, investigation of the kinematics of new data with better spectral and spatial sampling is mandatory.

### 1.2.2 An impact from the environment ?

Theoretical modelling based on simple physics principles such as angular momentum conservation, viscous friction, dissipation of energy or gravitational instabilities can account for both the global morphology and kinematics of galaxies. Though state of the art N-body simulations including other components such as stellar feedback from supernovae, Active Galactic Nuclei (AGN) in the centre of galaxies with their outflows and inflows from filaments of gas in the large scale structure of the Universe, have shown that these new mechanisms have more impact on the kinematics than previously thought. Nevertheless, seeing more disturbed morphologies and systems with high velocity dispersion at high redshift seems consistent with the hierarchical growth of dark matter haloes which drive the evolution of galaxies. In this regard, and as haloes will bound galaxies and gas together, we might expect to find a larger fraction of unrelaxed interacting and/or merging galaxies in groups and clusters than for field galaxies, that is those which do not belong to any structure.

Galaxies Star Formation Rate (SFR) will also depend on their redshift and their environment. This is sometimes computed through a scaling law with some gas density (generally neutral hydrogen HI) after accounting for dust attenuation, or by computing a Star Formation History (SFH) through Spectral Energy Distribution fitting techniques (requiring a spectrum). As stated above, the star formation is very different nowadays from the past. If we look back in time, we observe an increasing average SFR, reaching a peak around  $z \sim 1.5 - 2$  and then decreasing again. This is partially linked to the fact that we observe a larger fraction of spheroidal systems with high SFR than in the local Universe.

---

<sup>1</sup>We will preferentially use the terms disk-like/late-type galaxies rather than spiral as some galaxies studied in the present work do show a disk morphology without clear spiral arm patterns.

Star formation only occurs when there is enough gas supplies to locally gather into collapsing clouds. Once all the gas has been consumed, the SFR is expected to quickly drop to 0 and the galaxy becomes quenched. The question of the impact of the environment on these quenched galaxies we see today is of uttermost importance. Indeed, we expect galaxies found in groups and clusters to lie in rich hot gas environments which might be filled with inflows from filaments of gas observed in the large scale structure, or with the galaxies gas content. In the former case, this would imply higher rates of star formation in groups as there is a constant fuelling of gas. On the other hand, if the gas comes from the galaxies through physical processes such as ram pressure stripping, we should see less star forming galaxies in these regions as they might have lost a significant fraction of their content. Isolated field galaxies shall not be stripped of their gas, unless maybe if they are interacting with another galaxy at some point, though such interactions are more rare in these low density regions of the Universe. However, they will also lack inflows of gas, so we might expect to see them quench earlier than their groups and cluster counterparts.

### 1.3 Observation techniques in astronomy

#### 1.3.1 Spectroscopy and photometry

Studying the formation and evolution of galaxies requires large datasets of objects at low and high redshifts. The two types of observation which can be carried out to answer these questions are photometry and spectroscopy. These methods originally yielded different information on the properties of galaxies such as their light distribution, their morphology or the kinematics. Photometry provides 2D images of galaxies whose surface brightness, that is its total flux divided by its solid angle on the sky, is above the surface brightness limit imposed by the instrument limitations, but also whose size is above the instrument resolution. Depending on the band used, we can observe different galactic components, ranging from the cold, hot and ionised gas to young/old stellar populations, as well as dust. On the other side, spectroscopy gives us information on the importance of these components with respect to the total emitted light by looking at continuum, emission and absorption lines. Galaxy spectra can contain high continuum values coming from the combination of old and young stellar populations spread through the galaxy. Detected emission lines, such as  $H\alpha$ ,  $H\beta$ , [OII] and [OIII] doublets or  $Ly\alpha$  give us insight into the existence of gas and its ionisation, which can in turn indicate the presence of star-forming zones within the galaxy such as HII regions. On the contrary, absorption lines tell us about the existence of dust and gas on the line of sight which can be either outside of the galaxy, or directly inside (self-extinction).

From 2D images we can derive morphological parameters such as the ellipticity  $e = 1 - b/a$ , with  $b$  and  $a$  the minor and major axes respectively, or some measure of a

characteristic radius. Generally, it is assumed that the galaxies light profile has high degrees of symmetry. This implies that a galaxy with an inclination<sup>2</sup>  $i = 0^\circ$  should have circular isophotes (lines of identical surface brightness). When elliptical isophotes are seen, which implies an elliptical shape for the galaxy, this is an indication of a non-zero inclination. Based on our definition, this translates in terms of ellipticity as

$$\cos i = 1 - e \quad (1)$$

This assumption is invalid in reality as galaxies have more complex morphologies with central bars, spiral arms, satellite galaxies for the largest ones and potential inflows and/or outflows. It is also incorrect when we study galaxies which have clear disturbed morphologies due to past interactions such as merging events.

In the past, measuring radii and ellipticity were generally done by with a curve of growth, consisting in deriving the size and ellipticity of ellipses at different isophote levels. Nowadays, it has become common to fit galaxy light profile models onto images and to recover the morphological parameters from the best fit. One of the most commonly used light profile is a Sérsic profile which is generally written as (Graham et al., 2005)<sup>3</sup>

$$I(r) = I_e e^{-b_n \left( \left( \frac{r}{R_e} \right)^{1/n} - 1 \right)} \quad (2)$$

where  $r$  is the radial distance to the morphological centre of the galaxy,  $n$  is referred as the Sérsic index of the galaxy,  $R_e$  is the effective or half-light radius which encloses 50% of the total luminosity of the galaxy,  $I_e$  is the intensity at the position  $R_e$  and  $b_n$  is a term which ensures that  $R_e$  does enclose half the total luminosity. By integrating Eq. 2 up to infinity to recover the total luminosity  $L_{\text{tot}}$  and a second time to  $R_e$  so that it equals  $L_{\text{tot}}/2$ , one can find the definition of  $b_n$  to be such that

$$2\gamma(2n, b_n) = \Gamma(2n) \quad (3)$$

with  $\gamma$  and  $\Gamma$  the incomplete and complete gamma functions respectively.

This equation has been widely used in different contexts because of its ability to recover two famous profiles (a) an exponential disc for  $n = 1$  which represents a disk-like/spiral galaxy. Here,  $r$  is the radial distance in the galactic plane. Sometimes, two exponential discs are used to represents the vertical variation of the emitted light as well as in the plane of the galaxy. (b) a de Vaucouleurs profile for  $n = 4$  which describes early-type galaxies. Depending on the author, only a single Sérsic profile with a freely varying Sérsic

---

<sup>2</sup>We define the inclination as the angle between the plane of the galaxy and the plane of the sky, or equivalently between the normal to the plane of the galaxy and the line of sight.

<sup>3</sup>The original definition  $I(r) \propto e^{-(r/\alpha)^{1/n}}$  from Sérsic (1963) was modified to Eq. 2 because of the immeasurable values  $\alpha$  took in practice.

index can be used, as is the case for softwares such as SExtractor (Bertin & Arnouts, 1996) or GIMD2D (Simard, 1998), or a combination of a bulge and a disk, with two fixed Sérsic indices, which is the case in GALFIT (Peng et al., 2002).

Galaxies spectra can have a noisy continuum emission which can make difficult the detection of specific lines. In general, astronomers look at spectral features such as Balmer or Lyman lines, or doublets to improve the confidence in their detection. However, spectroscopes only work in a certain spectral domain, and therefore any line falling out the instrumental range cannot be detected. When a certain component in a galaxy is observed, this requirement translates in terms of redshift through the equation  $\lambda_{\text{obs}} = \lambda_{\text{em}}(1 + z)$ . Thus, this implies that galaxies can only be detected in a certain redshift interval.

The detection of a line is done through line fitting on a continuum subtracted spectrum. In general, an algorithm finds the redshift of a galaxy by identifying recognisable spectral features and measuring their wavelength offset from their expected rest-frame wavelength. The higher the number of detected lines, the more confidence we have in the redshift. Once this is known, each line is fitted separately with a Gaussian shaped profile from which values of the flux and the dispersion are computed. The shape and dispersion of a line is due to many factors. For galaxies spectra, deviations to Gaussian profiles are not considered as these are negligible and not resolved yet. The dispersion is affected both by beam smearing effects and by the velocity dispersion of the particles on the line of sight. The former corresponds to a broadening of the intrinsic velocity dispersion because of the finite instrumental spectral resolution. On the other hand, the latter is the real dispersion in the particles velocity space because of local turbulent motion induced by energy injection, for instance from supernovae.

### 1.3.2 Long slit and early integral field spectroscopy

Before the advent of Integral Field Spectroscopy (IFS), which combines the advantages of both photometry and spectroscopy by providing a spectrum for every pixel in an image, early studies of the rotation curves of galaxies had been done with long slit spectroscopy. In this case, previously known galaxies from photometric surveys were observed with the slit of the spectrograph matching the morphological Position Angle (PA) of the galaxy. This technique therefore assumed that the morphological and kinematical PA are identical, which recent studies might have proven wrong in some cases. The first resolved observation of this kind at high redshift was performed by Vogt et al. (1996) with Keck Telescope. This shed the first light on the resemblance of the rotation curves between galaxies in our local Universe and those found up to  $z \sim 1$ . Studies of higher redshift galaxies ( $2 \lesssim z \lesssim 3$ ) were done on star forming UV-selected Lyman Break Galaxies

(LBG), whose flux drops in the U-band because of their redshifted Lyman break.

The very first 3D spectrographs observed one galaxy at a time because of the lack of a large Field of View (FoV) with good spatial resolution. In this sense, they were used as a spectroscopic follow up of already detected galaxies in photometric surveys. One of these spectrographs was the instrument SINFONI (Eisenhauer et al., 2003) mounted on the Very Large Telescope in Chile, working with both natural seeing and Adaptive Optics (AO). Its corresponding original survey SINS (Förster Schreiber et al., 2009) of 80 objects observed from 2003 to 2008 was one of the first large kinematical IFS survey of its kind. In the following years, other surveys were carried at intermediate and high redshift. These include the OSIRIS survey (Law et al., 2007) observed with OSIRIS IFS on Keck Telescope,

MUSE is an Integral Field Unit (IFU) mounted on the VLT in Chile which spans a  $1' \times 1'$  Field of View (FoV). Its wavelength range covers both the visual spectrum and the Near Infra-Red part (NIR), going from 4650 Å to 9300 Å. This instrument was built with the main purpose of performing blind searches of sources in the field. The wavelength range is well suited to detect the OII doublet in the redshift range 0.4, 1.4.

## 2 Sample selection

### 2.1 MUSE-GTO MAGIC

### 2.2 COSMOS field

Group ID <sup>1</sup>	Ra <sup>2</sup> J2000 (°)	Dec <sup>3</sup> J2000 (°)	Exposure <sup>4</sup> (hr)	Average seeing <sup>5</sup> (")	Total nb. galaxies <sup>6</sup>	Nb. field galaxies <sup>7</sup>
CGr32	NaN	NaN	$3 \times 4.35$	0.51 - 0.58	277	113
CGr34_d	149.87766	2.502331	5.25	0.63	74	46
CGr34_bs	149.87766	2.502331	4.75	NaN	74	46
CGr30_d	150.144225	2.065971	9.75	0.67	124	65
CGr30_bs	150.144225	2.065971	6.25	NaN	124	65
CGr84	150.057219	2.599744	5.25	0.59	92	51
CGr84-N	NaN	NaN	1	0.51	81	38
CGr114	149.994285	2.258044	2.2	0.68	64	45
CGr79	149.820686	1.821825	4.35	0.60	65	37
CGr28	150.218094	1.812667	1	0.62	49	29
CGr26	150.492767	2.069139	1	0.59	46	31
CGr61	149.728741	1.915987	1	0.64	43	29
CGr51	149.982756	1.801899	1	0.6 – 0.7	44	29
CGr23	149.790782	2.162648	1	0.68	51	32

Table 1: Main characteristics of the observed MUSE fields. Groups ending with \_d correspond to deep observations (full stacked OBs) and with \_bs correspond to best-seeing observations (only OBs with a seeing below 0.7"). The seeing is given for the [OII] wavelength at the group's average redshift. 1. MUSE group number, 2. Group centre's right ascension, 3. Group centre's declination, 4. Length of observations, 5. Average seeing during observation, 6. Total number of detected galaxies within MUSE FoV, 7. Number of field galaxies found by the FoF algorithm.

The point of the analysis is to perform a joint study of the morphology and the kinematics of field galaxies in the COSMOS area (Scoville et al., 2007) using respectively HST ACS images and MUSE data. To this end, a set of 12 galaxy structures (groups or clusters) was selected. The choice of the COSMOS area for this analysis was made because of the large number of multi-band photometric data available for the galaxies in this field and the presence of rich galaxy groups.

Guaranteed Time Observations (GTO) centred on the groups were performed from which 14 different MUSE Fields of View (FoV) of  $1 \times 1 \text{ arcmin}^2$  were obtained. Each is composed of multiple Observation Blocks (OB) of 40 – 60 min each with the Position Angle (PA) of the instrument rotated by 90° between consecutive exposures.

Most of the groups enter into one MUSE FoV, except for CGr32. Since this group is more extended than the others, three slightly overlapping FoVs were taken around

it. A couple of groups were also split into *deep* and *best-seeing* observations, the former combining all the OBs regardless of the average seeing in each OB, when the latter only kept OBs with an average seeing lower than  $0.7''$ .

The main characteristics of the observed FoVs, including the position of their centre, the exposure per FoV, the average seeing during the observation, the total number of galaxies and the number of field galaxies detected by the FoF algorithm are listed in Table 1.

These structures were chosen from (Knobel et al., 2009), (Knobel et al., 2012) catalogues. This ensured them to have both a large set of corresponding photometric data available from Laigle et al. (2016) catalogue and HST images with a much better resolution ( $0.03 \text{ arcsec/px}$  for HST and  $\approx 0.2 \text{ arcsec/px}$  for MUSE). A few galaxies in CGr30\_deep and around some stars might have also been detected within the data cubes but not in HST images. In the former case, the reason is that a blind source detection was performed with ORIGIN (Bacon et al., 2017) which can deblend sources even below the PSF. For the latter, this is because galaxies were detected in areas around stars which were masked when creating Laigle et al. (2016) catalogue.

## 2.3 Prior information on the galaxies

### 2.3.1 Galaxies in structures

This internship was planned to be similar in many aspects to what is doing V. Abril-Melgarejo, a 2nd year PhD student supervised by B. Epinat at LAM, Marseille. She studies the morphology and the kinematics of the galaxies within the structures observed with MUSE in the same fields as those we are using in this work. The main difference is that we are focusing on "field" galaxies when she only studies those in structures. To differentiate between group and field galaxies, a Friend of Friends algorithm (FoF) was run prior to my arrival on the galaxies in the MUSE fields. Thus, each galaxy was labelled either as belonging to a structure or as a "field" galaxies. Additionally, a morphological analysis had already been performed by V. Abril-Melgarejo with GALFIT on galaxies in structures only. Two Sérsic profiles with fixed Sérsic indices ( $n = 1, 4$ ) were used to describe these galaxies as a combination of a disk and a bulge component. Hence, their intensity can be written as

$$I(r) = I_{e,d} e^{-b_1 \left[ \frac{r}{R_d} - 1 \right]} + I_{e,b} e^{-b_4 \left[ \left( \frac{r}{R_b} \right)^{1/4} - 1 \right]} \quad (4)$$

where  $I_{e,d}$ ,  $I_{e,b}$  are the effective intensities of the disk and the bulge component respectively and  $R_d$ ,  $R_b$  their half-light radii.

Therefore, we already have in hand morphological information for roughly half of



the total sample including model parameters as described above, but also morphological parameters such as the ellipticity of the galaxies, the position angle of their kinematical main axis (which can be different from the morphological PA).

### 2.3.2 Morphological information from COSMOS catalogues

The total number of galaxies detected in the 14 MUSE fields in the COSMOS area is around 1000. Roughly half of them belong to structures and the other half are labelled as "field" galaxies. However, not all of them are useful to our study. Some may be too close to the edge for detection, others may be too noisy with a low SNR, or even too small, preventing any relevant kinematical modelling. It is thus mandatory to apply a selection on our data set of field galaxies, first to save time for the analysis, but also to reduce uncertainties.

Our goal is to perform a joint study of the morphology and the kinematics of these galaxies. The tools and the models for the kinematical modelling were already developed as they were used by V. Abril-Melgajero. On the other hand, fitting morphological models with software such as GalFit or SExtractor would have required additional time which we did not have. Hopefully for us, morphological modelling had already been performed on the galaxies in the COSMOS field, so we could focus on the kinematical part.

Morphological information for all the galaxies in COSMOS can be found in various catalogues and tables<sup>4</sup>. To start with, we decided to use the two most complete catalogues we could find, that of Tasca (maybe citation) and Cassata (maybe citation as well). Both catalogues contain morphological information including the central position of the galaxy, its half-light radius, concentration and asymmetry parameters, ellipticity, PA of the major morphological axis, and so forth for roughly 232000 galaxies. The authors obtained morphological information by running SExtractor on HST images of the galaxies in Laigle et al. (2016) catalogue.

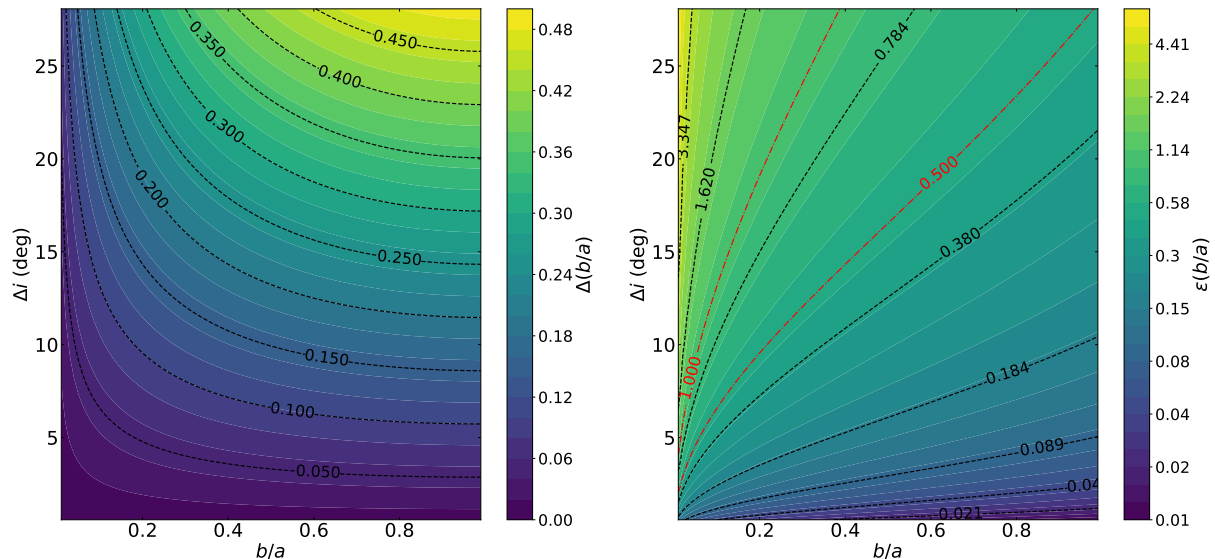
Since we already had in hand a catalogue combining spectroscopic information (emission line fluxes, redshift, etc.) from MUSE measurements with photometric data from Laigle et al. (2016), we cross-matched it with Cassata's and Tasca's tables to collect their morphological parameters. We cross-matched first with each catalogue separately, and then with both, using the right ascension  $\alpha$  and declination  $\delta$  of the centre of the galaxies, allowing for a maximum separation between the MUSE source and the closest source within the catalogues of 1 arcsec maximum. This procedure was done for structure galaxies as well in order to use them to check the consistency of the catalogues parameters.

---

<sup>4</sup><https://irsa.ipac.caltech.edu/data/COSMOS/tables/morphology/>

## 2.4 Checking catalogues values consistency

### 2.4.1 Reasons for checking catalogues values



(a) Error on inclination as a function of  $b/a$  and its absolute error. Contours of  $\Delta(b/a)$  are plotted in black dashed lines with their corresponding value. (b) Error on inclination as a function of  $b/a$  and its relative error. Contours of  $\epsilon(b/a)$  are plotted in black and red dashed lines with their corresponding value. Red contours correspond to values for which there is a 50% and 100% error on  $b/a$ .

Figure 1: Error on inclination as a function of  $b/a$  and its error. Left: as a function of the absolute error on  $b/a$  ( $\Delta(b/a)$ ). Right: as a function of the relative error on  $b/a$  ( $\epsilon(b/a)$ ). Red contours correspond to values for which there is a 50% and 100% error on  $b/a$ .

As a first step, we must select a sample based on relevant criteria. This is meant to ensure that we have reliable morphological and kinematical parameters and to reduce statistical errors. Given that any kinematical modelling relies on prior morphological information (galaxy centre, ellipticity, PA), we can only use a combination of values derived from spectral fitting, for instance the SNR, and from morphological modelling such as a measure of a galaxy radius to select our sample.

Before this internship, spectral fitting on the integrated spectra of the galaxies had already been done, and we combined our data with morphological information from COSMOS catalogues as discussed in the previous section. Potentially useful morphological information included half-light radii, magnitudes, ratios of minor to major axis ( $b/a$ ) or equivalently a measure of the ellipticity of the galaxies. Nevertheless, using this data without checking first how well it compares to values found in other catalogues and/or derived using different softwares/models could lead to high biases and uncontrolled errors. Thus, before discussing any selection criteria for our sample, we must first assess the reliability of the parameters we are going to use in later sections.

Important values to check are the half-light radius, as it will be used to select our sample, the  $b/a$  ratio and the PA since these are prior information for the kinematical modelling. We also checked that there was a correlation between GALFIT and the catalogues magnitudes. The axes ratio has a crucial importance since it is directly related to the inclination of the galaxy on the sky through Eq. 1. Given a certain error  $\Delta(b/a)$ , and using the usual formula for computing the error  $\Delta f = |\partial_x f| \Delta x$  of a function  $f$ , we find for the inclination

$$\Delta i = \Delta(b/a) \left| \frac{b}{a} \left( 2 - \frac{b}{a} \right) \right|^{-1/2} \quad (5)$$

This is illustrated in Fig. 1 where  $\Delta i$  has been plotted as a function of  $b/a$  and its error (absolute on the left, relative on the right). Contours of the error on  $b/a$  have been over-plotted to show how evolves  $\Delta i$  given a fixed error on  $b/a$ . As expected, the higher the error on  $b/a$  the higher the error on  $i$ . An error as high as 50% could yield  $\Delta i \approx 27^\circ$ , though this value is reached for  $b/a \approx 1$  where the axes ratio is the least constrained by the morphology. A more appropriate error on  $b/a$  of 20% gives a maximum  $\Delta i$  slightly above  $10^\circ$ , which is correct.

Since the inclination has a strong impact on the galaxy intrinsic maximum rotational velocity, and potentially on the classification of galaxies as rotationnaly supported or dispersion dominated, this indicates us that for any proper kinematical modelling we must check carefully that the values of axes ratios are consistent between catalogues.

#### 2.4.2 Catalogues used for comparison

As stated in previous sections, we cross-matched our catalogue of galaxies detected by MUSE in COSMOS with Cassata's and Tasca's, two tables with morphological information for the galaxies listed in Laigle et al. (2016). However, as can be seen in Fig. 5 and 4, we found large discrepancies between the parameters. Thus, to better understand their origin, we chose to cross-match our catalogue with another one also based on Laigle catalogue. This table has fewer HST counterparts of MUSE galaxies than in the other two but it contains additional morphological information which we can use for the comparison. In addition to that, we already had GALFIT morphological information on  $\sim 500$  group galaxies with strong confidence in their value. Therefore, we chose to compare the data in the three morphological catalogues with that of GALFIT.

#### 2.4.3 Total magnitudes

The first value we can easily compare is the apparent magnitude. Cassata's, Tasca's and Zurich's catalogues provide a measure of the total magnitude derived from fitting with SExtractor a single Sérsic profile with a free Sérsic index  $n$  on HST images.

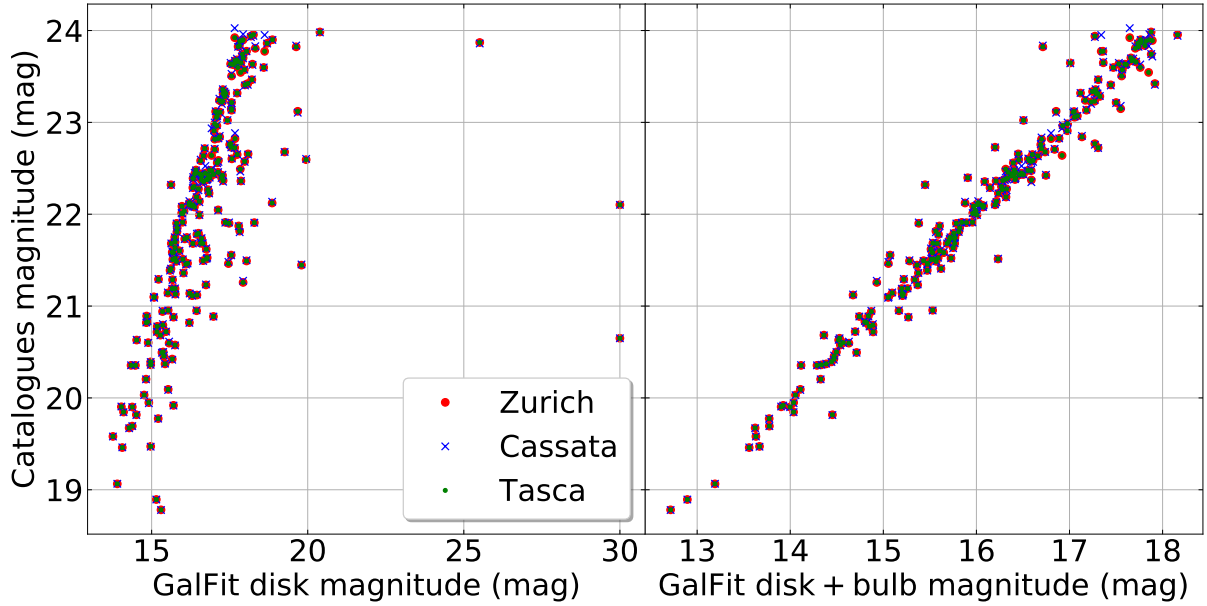


Figure 2: Comparison between the morphological catalogues magnitudes and that of GALFIT for cluster galaxies. Magnitudes from the catalogues agree well between each other. Left: compared with GALFIT disk magnitude only. The slope is too high and a few points are scattered far from the line. Right: compared with the total GALFIT magnitude as defined in Eq. 8. We find a linear relation with a scatter of about 1.6 mag.

Given that GALFIT galaxies light profile was modelled using two Sérsic profiles with fixed Sérsic indices ( $n = 1, 4$ ), we have two measures of their magnitude: one for the bulge component  $m_b^{\text{GF}}$ , and another for the disk component  $m_d^{\text{GF}}$ . To have a meaningful comparison between magnitudes, we need to compute the GALFIT total magnitude by combining the bulge and the disk components. Both are defined as

$$m_i^{\text{GF}} = -2.5 \log_{10} (F_i^{\text{GF}}) + C \quad (6)$$

where  $i = b, d$  represents either the bulge or the disk,  $F = L/4\pi D^2$  is the flux of the galaxy in some band,  $L$  its intrinsic luminosity,  $D$  its cosmological luminosity distance to us and  $C$  a constant depending on the band used.

Considering that the two components have different luminosities but are located at the same distance, we can add the fluxes together. Thus the total GALFIT magnitude can also be written as

$$m_{\text{tot}}^{\text{GF}} = -2.5 \log_{10} (F_b^{\text{GF}} + F_d^{\text{GF}}) + C \quad (7)$$

Inverting Eq. 6 to get the components flux as a function of their magnitude and inserting it into Eq. 7 yields

$$m_{\text{tot}}^{\text{GF}} = -2.5 \log_{10} \left[ 10^{-\frac{m_b}{2.5}} + 10^{-\frac{m_d}{2.5}} \right] \quad (8)$$

This is the value that should be compared with the three catalogues magnitudes. Fig. 2 shows how these scale with each other and with GALFIT disk magnitude on the left, and the total magnitude from Eq. 8 on the right. As expected, the catalogues give the same value except for a few points. We see that the total GALFIT magnitude gives a much better, poorly scattered linear relation with the catalogues magnitudes. Even though there is an offset between GALFIT and the catalogues, this is due to using different conventions for the constant term in Eq. 6.

The same comparison was done on field galaxies, except we did not have GALFIT magnitudes in this case. We also found a good agreement between the catalogues magnitudes.

#### 2.4.4 Morphological type classification

We might expect to have some discrepancies in our data because of the models used between GALFIT and SExtractor/GIM2D. A way to check this effect is to study how these differences scale with the morphological type of the galaxies. For instance, if we use the disk half-light radius of GALFIT to compare with that of SExtractor, we might expect to have some scatter in our relation for the elliptical galaxies as the disk component is not the best one to describe them.

To see how these relations scale with morphological types, we can use the classification given in the three morphological catalogues. These classifications are based on methods which can be quite different and which can use morphological parameters in different ways. A more detailed explanation of the parameters used, of how these methods work, of their strength and weaknesses can be found in

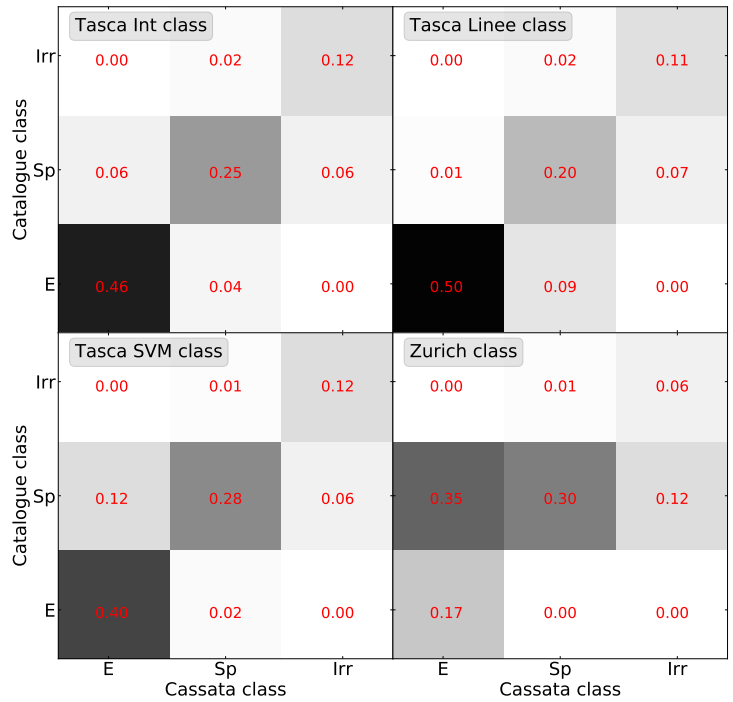


Figure 3: Comparison between morphological types given in Tasca and Zurich catalogues against that of Cassata. Galaxies are labelled as follows: E for ellipticals, Sp for spirals/disks-like, Irr for irregulars. The percentage of galaxies falling into the given classes is indicated in red and the method compared with Cassata's is shown on the top left corner of each plot. We find good agreement between Tasca and Cassata types but not between Cassata and Zurich.

Appendix A. We provide below a short introduction to these classifications:

- Cassata’s catalogue gives a classification based on morphological parameters they derived with SExtractor. To do so, they use a reference of 500 galaxies with known parameters which they visually classify as either elliptical, disk-like/spiral or irregular. From this set, each time a new galaxy must be classified, its 11 closest neighbours are inspected and the most frequent class is assigned to the galaxy.
- Tasca’s catalogue gives different classifications based on three methods. The first one is similar to the one used by Cassata. This is also the classification they recommend to use because this is the one they put the more their trust in. The second one uses the technique described in (insert Abraham 1996 here) using the asymmetry and concentration parameters. The last one uses a support vector machine to classify galaxies.
- Zurich’s catalogue gives a single classification called Zurich Estimator of Structural Type (ZEST) which is described in (Scarlata et al., 2007). This method is based on a Principal Component Analysis (PCA). They decided to keep the first three Principal Components (PA) which retain most of the information present in the original five parameters (concentration, asymmetry, Gini coefficient, second-order moment of the brightest pixels producing 20% of the total flux and the ellipticity of the galaxy).

The morphological types given in Tasca’s and Zurich’s catalogues are compared against the class given by Cassata in Fig.3. We observe a good agreement between Cassata’s and Tasca’s types with just a few elliptical galaxies labelled as disk-like and vice versa. Roughly 50% of the galaxies appear to be elliptical. On the contrary, Zurich’s classification seems to label more than 70% of the galaxies as disk-like, including a large number of elliptical galaxies .

Considering the recommendation of Tasca to use its Int class and since we find a good agreement between Cassata’s morphological type and those given by Tasca, we decided to use and to stick to Cassata’s class throughout this work whenever we needed to separate galaxies between elliptical/disk-like/irregulars. This choice also ensured us to have the largest sample possible with a coherent classification as Cassata’s catalogue is the one with the largest number of HST counterparts of MUSE galaxies in the COSMOS field. Because of the incompatible results between Zurich’s and Cassata’s/Tasca’s types, we decided to put aside these values and not use them, though this shall require further investigation in future work to assess the origin of these discrepancies.

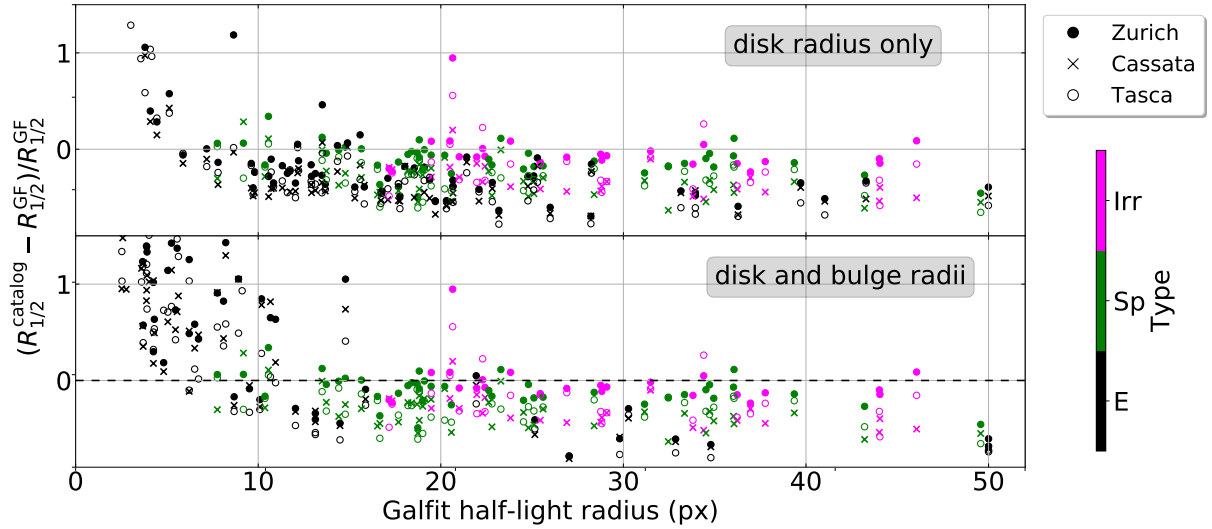


Figure 4: Relative error on the half-light radius between the catalogues and GALFIT. Points have been colour coded according to their classification given in Cassata’s catalogue (Irr for irregular, Sp for spiral/disk, E for ellipticals). Top: GALFIT disk radius is used for all the points. We observe an underestimation of the catalogues radius with respect to that of GALFIT for elliptical galaxies. Bottom: same plot with GALFIT bulge radius used for elliptical galaxies. In this case, we find an overestimation of the radius.

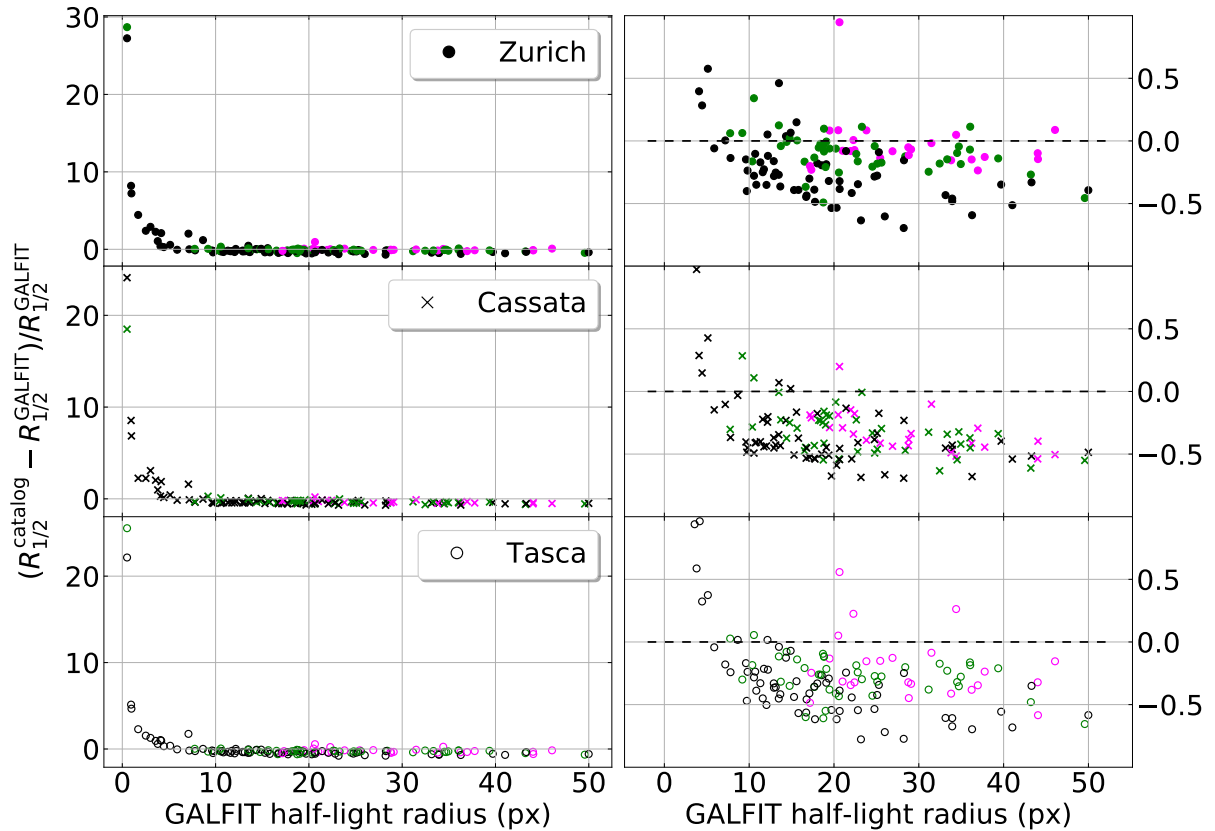


Figure 5: Comparison between half-light radii from the morphological catalogues and the radius of GALFIT disk component. This plot is similar to Fig.4 top plot but each catalogue was separated in its own subplot. Left: full range of relative error. Right: a zoom on the points with  $R_{1/2}^{GF} \geq 5$  px.

### 2.4.5 Half-light radii

Perhaps the most important parameter we have to check is the half-light radius. Indeed, if we underestimate it, we might remove from our sample resolved galaxies and therefore reduce our statistics. On the other hand, overestimating it would give us too many unresolved galaxies for which we would spend time removing noise dominated pixels without being able to perform their kinematical analysis in the end. Hence, it is mandatory to thoroughly check the values of the half-light radius from the three catalogues against that of GALFIT, and understand the origin of any discrepancies if there happens to be some.

We found a quite large disagreement between GALFIT half-light radius and those given in the morphological catalogues, as well as between them. This is illustrated in Fig. 4 and 5 where half-light radii in the catalogues are compared against that of GALFIT. Galaxies are colour coded according to the classification given in Cassata’s catalogue. We checked that using Tasca’s classifications as described in Sec. 2.4.4 did not change our conclusions. In these plots, we decided to use for the x-axis the half-light radius of the GALFIT disk component  $R_{1/2,d}^{GF}$  for all the galaxies, even though we might expect the ellipticals to be better described by their GALFIT bulge half-light radius. This choice is further discussed below.

The catalogues radii seem to be overestimated with respect to that of GALFIT for low  $R_{1/2,d}^{GF}$ . These are computed with SExtractor and, given that it does not take into account the PSF in its fitting routine, we expect the PSF to dominate for galaxies with small angular sizes. On the contrary, GALFIT does take into account the PSF in its calculation, and therefore we expect its half-light radius to decrease with lower values of  $R_{1/2,d}^{GF}$ .

When focussing on galaxies with a GALFIT radius larger than the HST-ACS PSF FWHM which is around 0.15" (4 – 5 px), we observe a global underestimation for all the catalogues, up to roughly 50%. This scatter is mainly due to elliptical galaxies. On the contrary, radii of disk-like galaxies have the least scatter and bias, especially the values given in Zurich’s catalogue. This different behaviour between elliptical and disk-like galaxies might be explained, as mentioned above, by the fact we are using the half-light radius of GALFIT disk component to assess the reliability of the elliptical galaxies radii give in the catalogues. A better choice may be to use the bulge component, which better describes the light profile of an elliptical galaxy, and its half-light radius for this population.

If we decide to split the galaxies into two categories, ellipticals and disks/irregulars, and if we use for the first category the bulge radius  $R_{1/2,b}^{GF}$ , and for the second  $R_{1/2,d}^{GF}$ , we



find that elliptical galaxies half-light radii from the catalogues are now overestimated as shown in Fig. 4 lower panel. These results suggest that elliptical galaxies in this sample are neither dominated (in terms of radius) by the disk component, nor by the bulge in the GALFIT model. Even though we did not push further the analysis on this discrepancy, we still mention that the next step should be to directly compute the half-light radius of the GALFIT model by integrating Eq. 4 up to half its total luminosity.

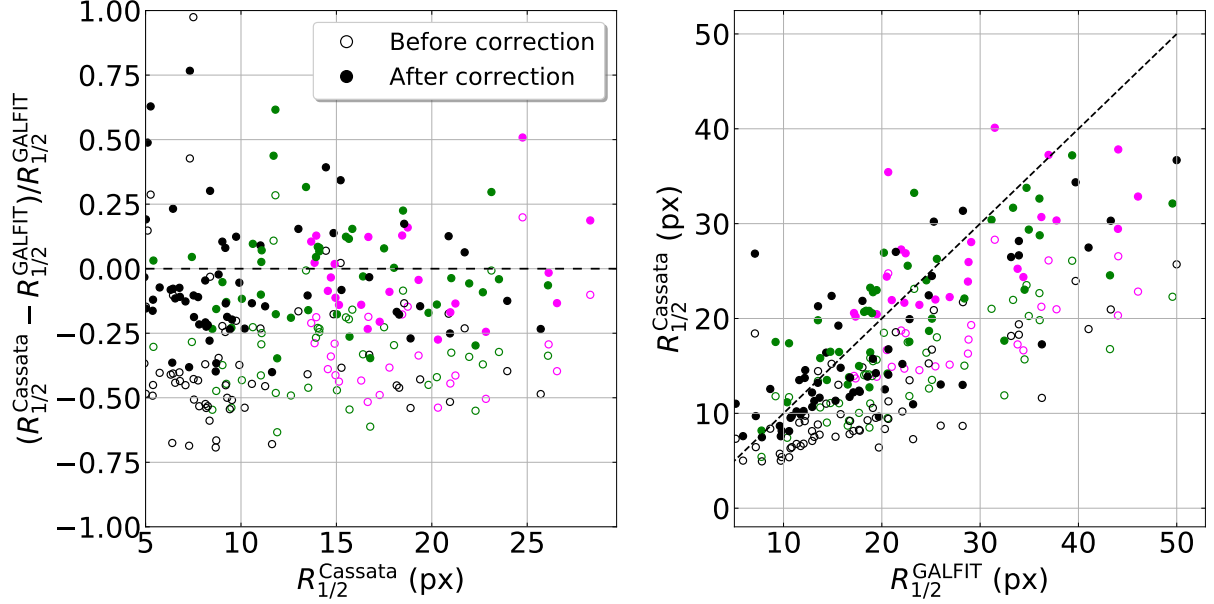


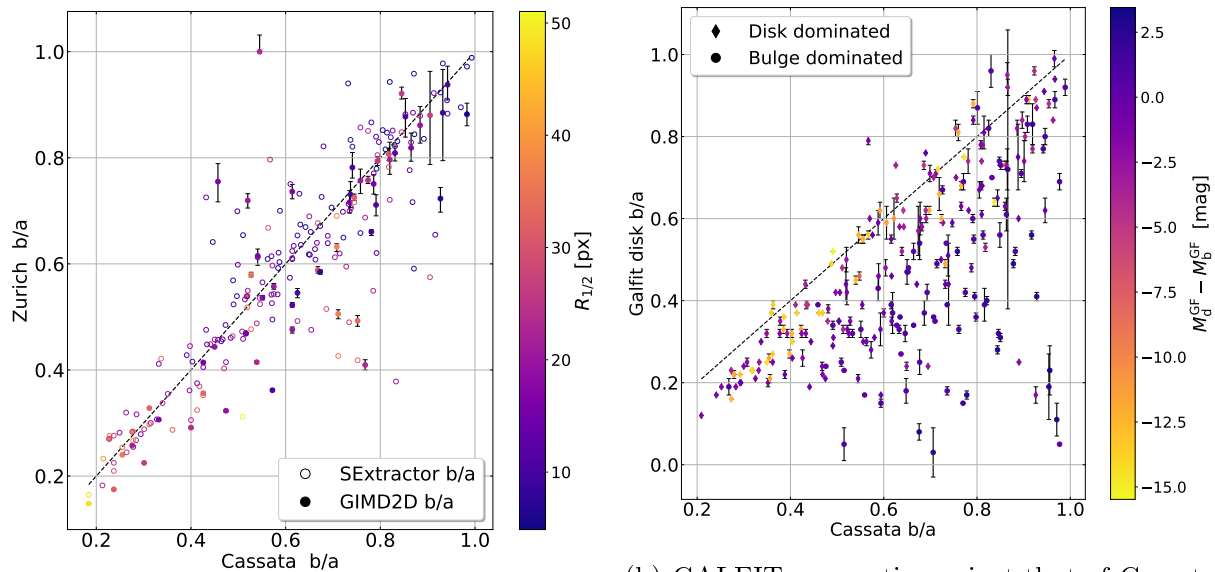
Figure 6: Bias and scatter before and after applying the correction mentioned in the paragraph. Left: half-light radius relative error as a function of Cassata’s radius. Right: scaling between Cassata’s and GALFIT radii. The scatter around 0.2px is not significantly changed after the bias correction.

Based on Fig. 5, we decided to use the galaxies half-light radii given in Zurich catalogue, keeping in mind that we might have a non-negligible fraction of elliptical galaxies for which their value may be underestimated. However, this is the catalogue with least HST counterparts. Thus, in order to increase our sample, we also chose to select additional galaxies found in Cassata’s catalogue but not in Zurich’s. As it seems that Cassata’s radius is more bias than Zurich’s, we fitted a linear relation onto the relative error data, which translates as

$$R_{1/2}^{\text{Corrected}} = R_{1/2}^{\text{Cassata}} (1 + \beta + \alpha R_{1/2}^{\text{Cassata}})^{-1} \quad (9)$$

where  $R_{1/2}^{\text{Corrected}}$  is the new half-light radius after the bias correction and  $\alpha, \beta$  the parameters of our fit. Based on previous arguments, we only fitted galaxies for which  $R_{1/2}^{\text{GF}} > 5$  px. Once a best fit solution was found, we slightly adjusted it by applying weights on ellipticals in order to limit their impact on disk-like galaxies radii which appeared to be too much overestimated. We found  $\alpha = 1.95 \times 10^{-3}$  and  $\beta = -0.349$ , which gives us 261 field galaxies with a radius either from Zurich or from the corrected value of Cassata.

### 2.4.6 Ellipticity



(a) Axes ratio from Zurich and Cassata for the field galaxies. There is an overall good agreement between the catalogues and between Zurich and GIM2D. We find a similar dispersion for SExtractor and GIM2D of about 0.1. No specific trend is found with the galaxies size.

(b) GALFIT axes ratio against that of Cassata for galaxies in structures. Globally, the axes ratio in the catalogue seems to be underestimated. If we separate the galaxies as disk or bulge dominated according to the most luminous component, we find that most of the scatter comes from elliptical galaxies.

Figure 7: Comparison between Cassata, Zurich and GALFIT  $b/a$  axes ratio. Zurich catalogue gives two values computed with SExtractor and GIM2D, and Cassata only with SExtractor. Error bars are only available for a few GIM2D and GALFIT values.

As mentioned in previous sections, the ellipticity is a critical parameter which is used to compute a value for the inclination of the galaxies. It is related to the  $b/a$  ratio given in the catalogues, so we can compare it as a proxy for the ellipticity. This is illustrated in Fig. 7 (a) where the axes ratio is compared for field galaxies for which we could assign a radius as described in Section 2.4.5 (b) GALFIT  $b/a$  is compared with that of Cassata for structure galaxies. Catalogues give consistent values for field galaxies with most of the scatter coming from the region where  $0.4 < b/a < 0.8$ . We checked that the size of the galaxies did not impact too much on the error, but we did not find any specific trend. We also checked that catalogues values are comparable to that of GALFIT. In this case, we find a large scatter with the catalogues axes ratio underestimated with respect to GALFIT value for almost all galaxies. Since GALFIT fits two components on the light profile, we expect the galaxies with a dominant bulge to have a less constrained  $b/a$  ratio. To check this effect, we colour coded the points according to the difference in magnitude between GALFIT disk and bulge components  $M_d^{GF} - M_b^{GF}$ . We observe that the majority of the scatter actually comes from bulge dominated galaxies, i.e. ellipticals, for which  $M_d^{GF} - M_b^{GF} > 0$ .

## 2.5 SNR and size selection

### 2.5.1 Size selection

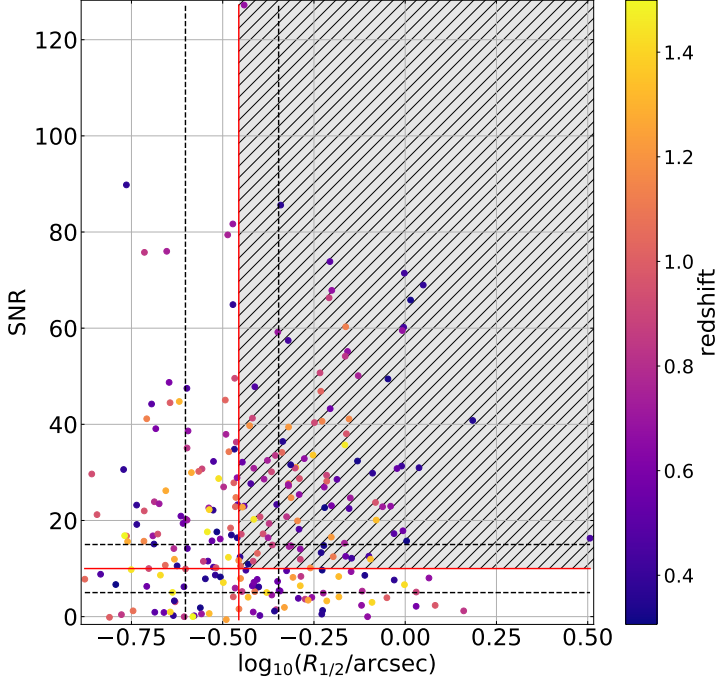


Figure 8: Full sample of 261 field galaxies with our selection box over-plotted (hatched area). Galaxies with  $5 \leq \text{SNR} \leq 15$  and  $0.25'' \leq R_{1/2} \leq 0.45''$  (bounds plotted as dashed lines) were visually inspected to check how many resolved galaxies we might have lost. Selection criteria from Sec. 2.5 are also plotted as solid red lines. No specific trend appear with redshift.

The first parameter we can think of to make our selection is the size of the galaxies. We already checked in Section 2.4.5 biases which might arise, investigated their origins, and corrected them. Now that we have reliable values, we need to define a selection criterion. Based on Bacon et al. (2015) and Bacon et al. (2017), the MUSE Point Spread Function (PSF), that is the pattern we obtain when we observe a point-like source with MUSE, can either be described by a Moffat (1969) or a Gaussian profile. In practice, they showed that a Gaussian best fits the PSF for MUSE images, so we used this profile in the following parts whenever we needed the PSF.

The PSF Full Width at Half Maximum (FWHM) is directly related to the seeing conditions, and it can be easily derived from the relation  $I_{\text{PSF}}(\text{FWHM}/2) = I_0/2$ . Since it gives us information about the minimum spatial extent within which we start to lose information, we could use it as a starting point for our selection criterion. Moreover, we will need a reliable measure of the FWHM for each galaxy when performing the kinematical modelling. Indeed, according to the aforementioned articles the value of the FWHM is expected to linearly decrease with wavelength. All galaxies are observed via their [OII]  $\lambda\lambda 3729, 3729 \text{ \AA}$  doublet at the same rest-frame wavelength. But, given that they are all field galaxies located at a different redshift  $z$ , we actually observe them at wavelengths covering the entire MUSE spectrum, that is we have the usual relation  $\lambda_{\text{obs}} = \lambda_{\text{em}}(1+z)$ , where  $\lambda_{\text{em}}$ ,  $\lambda_{\text{obs}}$  are the emitted (rest-frame) and observed wavelengths respectively. Therefore, there is not just one FWHM value per field, but one per galaxy.

To derive this value, we need to compute the linear evolution in each field by measuring the FWHM of stars for at least two different wavelengths. Assuming seeing conditions are similar within a field (no spatial dependence), we can use the same relation per MUSE field to compute the FWHM for the [OII] wavelength at the redshift of the galaxies. These measures had already been done by B. Epinat and V. Abril-Melgajero on at least two stars per field.

Though a more rigorous modelling of the wavelength variation of the PSF FWHM including both more data points and potentially higher order terms is mandatory for future analysis, we decided to stick to this values in the present work, keeping in mind the uncertainties which will affect the velocity dispersion maps in the modelling section. A representation of the FWHM variation with wavelength for the 16 observations is shown in Fig. 11. Most MUSE fields have FWHM values below  $0.7''$  which is not surprising given that it was one of the constraints of the observations. CGr23 is the only FoV to have its FWHM above  $0.7''$  for almost every wavelength. Only galaxies further than  $z \approx 1.11$ . In Table. 1, the seeing is the average over the OBs for the [OII] doublet at the redshift of the group which is around 1.17. Hence the value below  $0.7''$ .

To have a criterion which is not galaxy dependent, we decided to keep galaxies with  $2R_{1/2} \geq 0.7''$  since this corresponds to an upper limit for the FWHM for almost every field. Moreover, according to Swinbank et al. (2017) who compared the half-light radius of the nebular [OII] emission in MUSE images with that of their HST counterpart in ACS *I* or WFC3 *H*-band, the [OII] half-light radius seems to scale with the HST radius as

$$R_{1/2}^{\text{OII}} = (1.18 \pm 0.03) R_{1/2}^{\text{HST}} \quad (10)$$

Thus, by using an upper limit, we might loose a few galaxies which might have been resolved enough. Nevertheless, this was mandatory if we wanted to keep a sample not too large given the time constraints.

### 2.5.2 SNR selection

The other information we use to select our sample is the signal to noise ratio. The SNR is generally derived as the ratio between the source's signal and the background level. The noisier an image, the lower the SNR is. Given that galaxy pixels dominated by noise will be removed before the modelling by an automatic cleaning routine, we would like to keep galaxies with a high enough SNR, so that there is still a significant amount of pixels after the cleaning.

In the MUSE pipeline, PLATEFIT (Tremonti et al., 2004) was run on the integrated

spectrum of the galaxies after deriving their redshift. This software uses a set of stellar spectra from Bruzual and Charlot (2003) and Sánchez-Blázquez et al. (2006) to fit and remove the continuum emission at the galaxy redshift. Each line is then fitted by a Gaussian profile individually with the same velocity offset and dispersion for all the lines. PLATEFIT returns galaxies spectral parameters such as the [OII] flux. From these, we used the flux and its error to compute a value for the SNR as

$$\text{SNR} = \frac{[\text{OII}] \text{ flux}}{[\text{OII}] \text{ flux error}} \quad (11)$$

Since the typical SNR value used by the routine we run to remove noise dominated pixels in the MUSE maps is around 5, we decided as a first step to choose an SNR lower limit of 10, allowing us to keep galaxies with strong enough detection after the automatic cleaning is performed.

## 2.6 Characterisation of the sample

### 2.6.1 Selecting galaxies

We decided to visually inspect galaxies around the SNR and the size cuts to quantify (a) how many resolved galaxies would be lost if we applied the criteria given in Sec. 2.5.1 and 2.5.2 (false negative) (b) how many unresolved galaxies would be selected in our sample (false positive). To do so, we defined four boxes:  $5 \leq \text{SNR} \leq 10$ ,  $10 \leq \text{SNR} \leq 15$ ,  $0.25'' \leq R_{1/2} \leq 0.35''$  and  $0.35'' \leq R_{1/2} \leq 0.45''$  containing 46, 20, 58 and 49 galaxies respectively.

We then ran an automatic cleaning routine for all the galaxies in these boxes. This algorithm removes any pixel which either has its SNR below 5 or a dispersion below a certain percentage  $\gamma$  of the velocity dispersion  $\sigma_v$  computed from the Line Spread Function (LSF) FWHM. The LSF corresponds to the spectral equivalent of an image PSF, and tells us how much the instrument will broaden out an infinitely thin line. According to (Bacon et al., 2017) and (Guérou et al., 2017) who measured

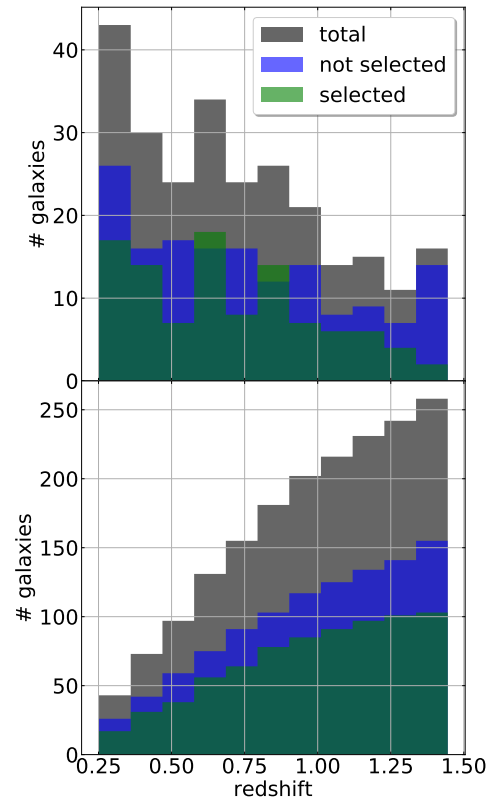


Figure 9: Redshift distribution of the total sample (grey), selected (green) and unselected (blue) galaxies. Redshift bins of size 0.1 have been used. Top: density plot as a function of redshift. Bottom: cumulative distribution. We lack most of the galaxies at redshift 1.4. Other redshift bins do not loose to many galaxies with respect to the unselected ones except maybe at  $z \approx 0.5$ .

the LSF variation with wavelength in the Hubble Ultra Deep Field (HUDF) and Hubble Deep Field South (HDFS) and who showed that it was stable through time, we computed the LSF FWHM as

$$\text{FWHM} = a\lambda^2 + b\lambda + c \quad (12)$$

with  $a = 5.866 \times 10^{-8} \text{\AA}^{-1}$ ,  $b = -9.187$ ,  $c = 6.040 \text{\AA}$  and  $\lambda$  the observed wavelength. Thus, the LSF FWHM will depend upon the redshift of the galaxy as well. It is related to the velocity dispersion via

$$\frac{\sigma_v}{c} = \frac{\sigma}{\lambda_{\text{em}}(1+z)} \quad (13)$$

where  $\sigma = \text{FWHM} (2\sqrt{2\log 2})^{-1}$  is the spectral dispersion due to the LSF.

The choice to keep pixels with a velocity dispersion above  $\gamma\sigma_v$  was motivated by the fact that sky lines from OH molecules in the atmosphere can generate false [OII] emission lines. Sky subtraction during the data reduction can also add new lines in the MUSE images. However, these are always found to have a width below the LSF FWHM. So any pixel with a false detection will be removed with this choice. The percentage  $\gamma$ , which we chose to be 80%, is meant to not remove pixels with real detection which might have thin lines.

After visually inspecting their sizes in the cleaned maps, we classified them as resolved or not. These boxes, the SNR, half-light radius and redshift of the full sample of field galaxies before selection are shown in Fig.8. Among the 261 field galaxies, 103 fall into the limits imposed in Sec.2.5. We find that roughly 26% of the galaxies below the cuts are actually false negatives and that 15% above them are false positives. Since this classification is purely visual, slightly relaxing the constraints on to whether a galaxy is resolved enough or not allow these values to vary by roughly 10%. Our criteria for the selection therefore seem fine, though in future works we might increase our sample by a factor of  $\sim 1.5$  by visually inspected each galaxy separately.

### 2.6.2 Redshift distribution

The choice of the [OII]  $\lambda\lambda 3729, 3729 \text{\AA}$  doublet for the kinematical analysis was due in part to the large range of redshift it covered given the MUSE spectrum. We therefore had in our catalogue galaxies spanning a redshift range from 0.3 to about 1.4. As show in Fig.9, after our selection we loose a significant fraction of galaxies with  $z$  around 0.3, 0.5 and 0.75 as well as the majority of the most distant galaxies. It is not surprising

to loose galaxies at high redshift as these have the lowest angular sizes on the sky at a fixed physical length. Nevertheless, we are globally selecting less galaxies per redshift bin than we are putting aside. The average and median redshifts are 0.749 and 0.719 for the selected galaxies, 0.809 and 0.750 for the unselected ones. Thus, our sample remains consistent in terms of redshift even after the selection.

### 2.6.3 Mass-SFR relation

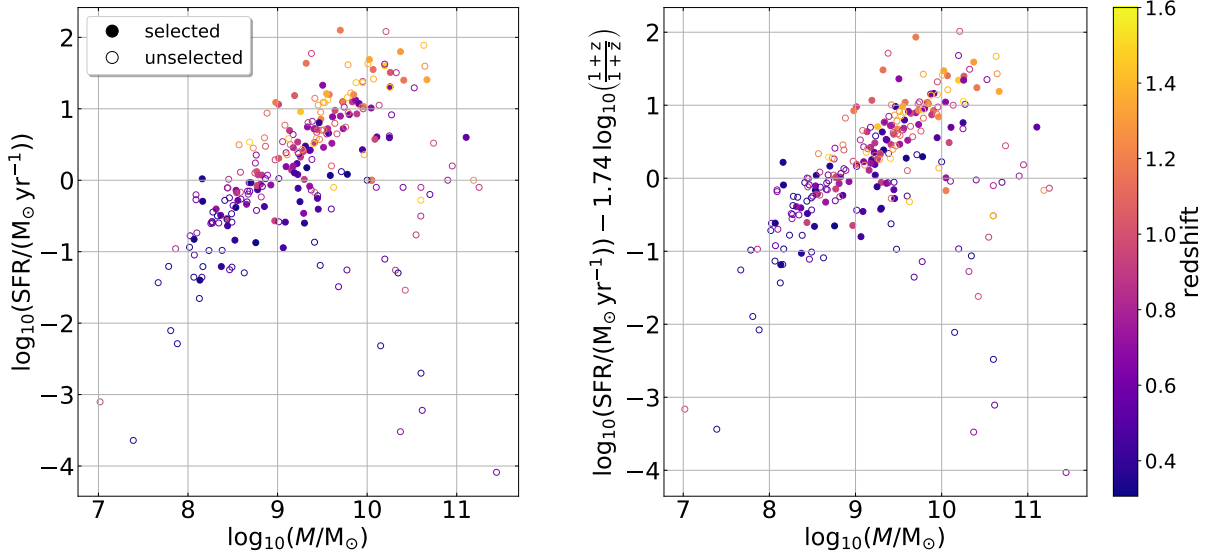


Figure 10: SFR-mass relation for selected (filled circles) and unselected (open circles) galaxies. Left: SFR extracted from the morphological catalogues. Right: the redshift corrected SFR as given in Eq.14. We obtain the usual main sequence of galaxies as a linear relation between SFR and mass (in log-log space), as well as quenched galaxies on the lower right part of the plane which are removed when performing the selection.

Our sample spans 3 orders of magnitude both in mass and SFR in the ranges  $10^{8.07} \leq M/M_{\odot} \leq 10^{11.1}$  and  $10^{-1.40} \leq \text{SFR}/(M_{\odot} \text{yr}^{-1}) \leq 10^{2.10}$ . We can investigate where our sample lies in the mass-SFR diagram as shown in Fig.10. Star-forming galaxies are expected to lie on a diagonal line with some scatter in  $\log M$ - $\log \text{SFR}$  space called the galaxies Main Sequence (MS) or the star-formation sequence. A few highly star-forming galaxies called Ultra Luminous InfraRed Galaxies (ULIRG/LIRG) are generally found above the main sequence. Some massive quiescent (low SFR values) galaxies can also be found below the MS. In our sample, we recover it after selecting the galaxies, but we loose the massive ones with low SFR values. This is probably due to the fact that we are selecting galaxies with a high enough [OII] surface brightness. Since [OII] flux comes from ionised regions which correlate with star formation, most quiescent galaxies are eliminated when observing, and the few large enough to be observed will have too low SNR values to be selected.

We also checked if there was any redshift evolution in the main sequence. We refer to Boogaard et al. (2018) who derived a redshift evolution for their galaxies on the MS found roughly in the same redshift, mass and SFR intervals. They modelled the log of the SFR as a plane in  $\log M$  -  $\log(1+z)$  space

$$\log_{10} \left( \frac{\text{SFR}}{\text{M}_{\odot} \text{ yr}^{-1}} \right) = 0.83^{+0.07}_{-0.06} \log_{10} \left( \frac{M}{\text{M}_{\odot}} \right) - 0.83^{+0.05}_{-0.05} + 1.74^{+0.66}_{-0.68} \log_{10} \left( \frac{1+z}{1+z_0} \right) \quad (14)$$

where  $z_0$  acts as a normalisation factor which will scale the relation at this redshift. We chose the median redshift of the selected galaxies to apply the SFR correction shown in the right plot of Fig. 10. Though we do not find a significant improvement in the scatter after the correction is applied.



### 3 Kinematical modelling

#### 3.1 Manual cleaning

For every selected galaxy, we ran the automatic cleaning routine as described in Section 2.6.1. Cleaned maps were produced and the velocity maps were visually inspected. Isolated pixels were removed even if they had a clearly visible [OII] doublet. We also inspected their line near the edges and we removed any pixel whose velocity seemed inconsistent with that of its neighbours (a single negative value around positives ones for instance). Twelve galaxies were unresolved and 3 were too close to the edges of the MUSE fields which resulted in missing data. Relaxing the SNR threshold in the routine to 3 allowed us to recover 6 galaxies out of 12.

#### 3.2 Kinematical parametrisation

The MUSE velocity maps only give us information about a single projected component of the 3D velocity field. Indeed, for a given pixel, the mean offset of the best fit Gaussian profile of the observed line is used in the usual Doppler shift formula to derive the velocity

$$\frac{\lambda_{\text{obs}} - \lambda_{\text{em}}}{\lambda_{\text{em}}} = \frac{v}{c} \quad (15)$$

with  $v$  positive if it recedes from us and negative if it approaches. This means the only measure we have is the radial component of the gas velocity within the pixels. If we use the same coordinate system as defined in Epinat et al. (2008), we can write the observed projected radial component  $V_{\text{obs}}$  as

$$V_{\text{obs}}((x_c, y_c), R, \theta, i, V_{\text{sys}}, \text{PA}) = V_{\text{sys}} + [V_{\text{rot}}(R) \cos \theta + V_{\text{exp}}(R) \sin \theta] \sin i + V_z(R) \cos i \quad (16)$$

where  $(x_c, y_c)$  is the galaxy centre position,  $R$  the radial distance in the galactic plane,  $i$  the galaxy inclination and PA the kinematical position angle (which might be different from the morphological one). In Eq. 16, the velocity components are (a)  $V_{\text{sys}}$  the systematic velocity due to the expansion of the Universe (b)  $V_{\text{rot}}$  the rotational velocity tangent to the plane of the galaxy (c)  $V_{\text{exp}}$  the expansion velocity oriented in the radial direction in the galactic plane (d)  $V_z$  the vertical velocity normal to the plane.

In practice, spectroscopic measurements give us  $\Delta V_{\text{obs}} = V_{\text{obs}} - V_{\text{sys}}$ . In Eq. 16, the dependence on the kinematical major axis position angle is implicit since  $\theta$  is defined as the angle in the galactic plane starting from the major axis. Thus,  $\theta = 0^\circ$  ( $90^\circ$ ) when we measure the velocity of a point on the major (minor) axis. The dependence on the galaxy centre position is also implicit as the radial distance is counted from this point.

Both  $R$  and  $\theta$  can be easily derived given  $(x_c, y_c)$  and the PA, but the inclination of the galaxy must be known in advance. Indeed, models tend to poorly converge when the inclination is left free to vary. More importantly, assuming the rotation curve along the major axis reaches a maximum rotational velocity or at least a plateau, we deduce from Eq. 16 that the maximum rotational velocity will scale as

$$V_{\text{obs}}^{\text{max}}(R_{\text{max}}, i) = V_{\text{rot}}(R_{\text{max}}) \sin i \quad (17)$$

where  $R_{\text{max}}$  represents the radius at which the maximum/plateau velocity is reached. Thus, just by looking at the rotation curve and by measuring its maximum value, we cannot raise the degeneracy between the inclination, which will lower the velocity, and the real maximum rotational velocity. Hence, it must be used as a fixed input.

### 3.3 Model

We deduce the kinematical parameters of our galaxies by fitting 2D velocity models onto the cleaned velocity maps. Though a few different models exist, some derived assuming a certain mass distribution, others purely based on visual inspections of the velocity curves, we focussed on a single model. We shall inspect how our conclusions might change if we use other models in future analysis.

This model we are using in this analysis consists in describing the rotation curve along the kinematical major axis as a linearly increasing slope in the central part, till reaching a turnover point whereafter the velocity remains constant. This relies on the assumption of a thin disk, which might no longer be true for nearly edge-on galaxies ( $75^\circ \lesssim i \lesssim 90^\circ$ ) due to the increasing depth leading to higher values of opacity. The second assumption is that there actually is a global rotation in our galaxies. In the local Universe, we know this might not be true for ellipticals. However, in our case, we expect spheroidal systems to still have some rotation, though it might be less significant.

We also do not take into account features such as a central bar, arms or clumps. The main reason is that we are lacking resolution to clearly see these effects in the kinematical maps. Some galaxies do show arms and clumpy components in HST images. However, even if the nebular emissions trace these structures, the MUSE PSF will blend them in a manner that all relevant information will be lost. Moreover, these structures are instability driven and the most distant galaxies in our sample are probably still unrelaxed systems. So, in this regard, we expect to see few of them at these redshifts.

In our case, we assume we have smooth velocity fields with no bar, no arms and no clumps such as HII regions. In our model, 4 morphological and 1 kinematical parameters are used. The inclination of the galaxy, its centre right ascension and declination and

the  $PA$  of the major axis must be given as fixed values. The kinematical parameter corresponds to the systematic velocity, that is the radial component of the velocity due to the expansion of the Universe.

### 3.4 Maximum velocity and velocity dispersion

The model returns the minimum, maximum, average and median values for the dispersion map once corrected of beam smearing effects. We also recover the rotational velocity on the plateau  $V_p$ , as well as the radius at which it is reached  $R_p$  and the maximum radius where the fit was performed  $R_{\text{last}}$ . If the model converges to  $R_p > R_{\text{last}}$ , the measure of both  $R_p$  and  $V_p$  are not reliable any more. Thus any galaxy meeting this condition is not considered in the following.

To remain consistent with other studies, we decided to compute the maximum velocity at  $2.2R_d$ , with  $R_d$  the disc scale length. This is defined as the radial distance in a morphological exponential disc model where the intensity drops by a factor of  $e$  with respect to the central value. From this definition, we can compute its scaling relation with  $R_{1/2}$ . Given that  $I(R_d) = I_0 e^{-1} = I_e e^{-b_1(R_d/R_e-1)}$ , we find

$$R_e = b_1 R_d \quad (18)$$

where  $b_1$  is the solution of the equation  $2\gamma(2, b_1) = \Gamma(2)$ . This also translates as

$$\int_0^x t e^{-t} dt = 1 - e^{-x}(1+x) = 1/2 \quad (19)$$

for which we find a solution by making the substitution  $x \rightarrow -y-1$  and using the Lambert W function

$$x = -W\left(-\frac{1}{2e}\right) - 1 \approx 1.67835 \quad (20)$$

where we only kept the positive, physically meaningful, solution.

## References

- Abraham, R. G., Valdes, F., Yee, H. K. C., & van den Bergh, S. (1994, Sep). The Morphologies of Distant Galaxies. I. an Automated Classification System. *Astrophysical Journal*, *432*, 75. doi: 10.1086/174550
- Abraham, R. G., van den Bergh, S., Glazebrook, K., Ellis, R. S., Santiago, B. X., Surma, P., & Griffiths, R. E. (1996, Nov). The Morphologies of Distant Galaxies. II. Classifications from the Hubble Space Telescope Medium Deep Survey. *Astrophysical Journal Supplement*, *107*, 1. doi: 10.1086/192352
- Bacon, R., Brinchmann, J., Richard, J., Contini, T., Drake, A., Franx, M., ... de Zeeuw, T. (2015, Mar). The MUSE 3D view of the Hubble Deep Field South. *Astronomy and Astrophysics*, *575*, A75. doi: 10.1051/0004-6361/201425419
- Bacon, R., Conseil, S., Mary, D., Brinchmann, J., Shepherd, M., Akhlaghi, M., ... Carollo, M. (2017, Nov). The MUSE Hubble Ultra Deep Field Survey. I. Survey description, data reduction, and source detection. *Astronomy and Astrophysics*, *608*, A1. doi: 10.1051/0004-6361/201730833
- Bershady, M. A., Jangren, A., & Conselice, C. J. (2000, Jun). Structural and Photometric Classification of Galaxies. I. Calibration Based on a Nearby Galaxy Sample. *The Astronomical Journal*, *119*(6), 2645-2663. doi: 10.1086/301386
- Bertin, E., & Arnouts, S. (1996, June). SExtractor: Software for source extraction. *Astronomy and Astrophysics Supplement*, *117*, 393-404. doi: 10.1051/aas:1996164
- Boogaard, L. A., Brinchmann, J., Bouché, N., Paalvast, M., Bacon, R., Bouwens, R. J., ... Zabl, J. (2018, November). The MUSE Hubble Ultra Deep Field Survey. XI. Constraining the low-mass end of the stellar mass - star formation rate relation at  $z < 1$ . *Astronomy and Astrophysics*, *619*, A27. doi: 10.1051/0004-6361/201833136
- Bruzual, G., & Charlot, S. (2003, Oct). Stellar population synthesis at the resolution of 2003. *Monthly Notices of the Royal Astronomical Society*, *344*(4), 1000-1028. doi: 10.1046/j.1365-8711.2003.06897.x
- Conselice, C. J. (1997, Nov). The Symmetry, Color, and Morphology of Galaxies. *Publications of the Astronomical Society of the Pacific*, *109*, 1251-1255. doi: 10.1086/134004

- Eisenhauer, F., Abuter, R., Bickert, K., Biancat-Marchet, F., Bonnet, H., Brynnel, J., ... Farinato, J. (2003, Mar). SINFONI - Integral field spectroscopy at 50 milli-arcsecond resolution with the ESO VLT. In M. Iye & A. F. M. Moorwood (Eds.), *Instrument design and performance for optical/infrared ground-based telescopes* (Vol. 4841, p. 1548-1561). doi: 10.1117/12.459468
- Epinat, B., Amram, P., Marcelin, M., Balkowski, C., Daigle, O., Hernandez, O., ... Balard, P. (2008, Aug). GHASP: an H $\alpha$  kinematic survey of spiral and irregular galaxies - VI. New H $\alpha$  data cubes for 108 galaxies. *Monthly Notices of the Royal Astronomical Society*, 388(2), 500-550. doi: 10.1111/j.1365-2966.2008.13422.x
- Förster Schreiber, N. M., Genzel, R., Bouché, N., Cresci, G., Davies, R., Buschkamp, P., ... Genel, S. (2009, Dec). The SINS Survey: SINFONI Integral Field Spectroscopy of  $z \sim 2$  Star-forming Galaxies. *The Astrophysical Journal*, 706(2), 1364-1428. doi: 10.1088/0004-637X/706/2/1364
- Graham, A. W., Driver, S. P., Petrosian, V., Conselice, C. J., Bershad, M. A., Crawford, S. M., & Goto, T. (2005, Oct). Total Galaxy Magnitudes and Effective Radii from Petrosian Magnitudes and Radii. *The Astronomical Journal*, 130(4), 1535-1544. doi: 10.1086/444475
- Guérou, A., Krajnović, D., Epinat, B., Contini, T., Emsellem, E., Bouché, N., ... Erroz-Ferrer, S. (2017, Nov). The MUSE Hubble Ultra Deep Field Survey. V. Spatially resolved stellar kinematics of galaxies at redshift  $0.2 \lesssim z \lesssim 0.8$ . *Astronomy and Astrophysics*, 608, A5. doi: 10.1051/0004-6361/201730905
- Hubble, E. P. (1922, Oct). A general study of diffuse galactic nebulae. *Astrophysical Journal*, 56, 162-199. doi: 10.1086/142698
- Hubble, E. P. (1926, Dec). Extragalactic nebulae. *Astrophysical Journal*, 64, 321-369. doi: 10.1086/143018
- Hubble, E. P. (1929, Jan). A Relation between Distance and Radial Velocity among Extra-Galactic Nebulae. *Contributions from the Mount Wilson Observatory*, 3, 23-28.
- Kent, S. M. (1985, Oct). CCD surface photometry of field galaxies. II. Bulge/disk decompositions. *Astrophysical Journal, Suppl. Ser.*, 59, 115-159. doi: 10.1086/191066
- Knobel, C., Lilly, S. J., Iovino, A., Kovač, K., Bschorr, T. J., Presotto, V., ... Welikala, N. (2012, Jul). The zCOSMOS 20k Group Catalog. *The Astrophysical Journal*, 753(2), 121. doi: 10.1088/0004-637X/753/2/121

- Knobel, C., Lilly, S. J., Iovino, A., Porciani, C., Kovač, K., Cucciati, O., ... Scaramella, R. (2009, Jun). An Optical Group Catalog to  $z = 1$  from the zCOSMOS 10 k Sample. *The Astrophysical Journal*, 697(2), 1842-1860. doi: 10.1088/0004-637X/697/2/1842
- Laigle, C., McCracken, H. J., Ilbert, O., Hsieh, B. C., Davidzon, I., Capak, P., ... Zabl, J. (2016, June). THE COSMOS2015 CATALOG: EXPLORING THE  $1 < z < 6$  UNIVERSE WITH HALF A MILLION GALAXIES. *The Astrophysical Journal Supplement Series*, 224(2), 24. Retrieved 2019-03-21, from <http://stacks.iop.org/0067-0049/224/i=2/a=24?key=crossref.13400bd5b9499f45ce2b1d44c4a48475> doi: 10.3847/0067-0049/224/2/24
- Law, D. R., Steidel, C. C., Erb, D. K., Larkin, J. E., Pettini, M., Shapley, A. E., & Wright, S. A. (2007, Nov). Integral Field Spectroscopy of High-Redshift Star-forming Galaxies with Laser-guided Adaptive Optics: Evidence for Dispersion-dominated Kinematics. *The Astrophysical Journal*, 669(2), 929-946. doi: 10.1086/521786
- Lotz, J. M., Primack, J., & Madau, P. (2004, Jul). A New Nonparametric Approach to Galaxy Morphological Classification. *The Astronomical Journal*, 128(1), 163-182. doi: 10.1086/421849
- Moffat, A. F. J. (1969, December). A Theoretical Investigation of Focal Stellar Images in the Photographic Emulsion and Application to Photographic Photometry. *Astronomy and Astrophysics*, 3, 455.
- Peng, C. Y., Ho, L. C., Impey, C. D., & Rix, H.-W. (2002, July). Detailed Structural Decomposition of Galaxy Images. *The Astronomical Journal*, 124, 266-293. doi: 10.1086/340952
- Perlmutter, S., Aldering, G., Goldhaber, G., Knop, R. A., Nugent, P., Castro, P. G., ... Project, T. S. C. (1999, Jun). Measurements of  $\Omega$  and  $\Lambda$  from 42 High-Redshift Supernovae. *The Astrophysical Journal*, 517(2), 565-586. doi: 10.1086/307221
- Riess, A. G., Filippenko, A. V., Challis, P., Clocchiatti, A., Diercks, A., Garnavich, P. M., ... Tonry, J. (1998, Sep). Observational Evidence from Supernovae for an Accelerating Universe and a Cosmological Constant. *The Astrophysical Journal*, 116(3), 1009-1038. doi: 10.1086/300499
- Rubin, V. C., Ford, J., W. K., & Thonnard, N. (1978, Nov). Extended rotation curves of high-luminosity spiral galaxies. IV. Systematic dynamical properties, Sa -> Sc. *Astrophysical Journal*, 225, L107-L111. doi: 10.1086/182804
- Rubin, V. C., & Ford, J., W. Kent. (1970, Feb). Rotation of the Andromeda Nebula from a Spectroscopic Survey of Emission Regions. *Astrophysical Journal*, 159, 379. doi: 10.1086/150317

- Sánchez-Blázquez, P., Peletier, R. F., Jiménez-Vicente, J., Cardiel, N., Cenarro, A. J., Falcón-Barroso, J., . . . Vazdekis, A. (2006, Sep). Medium-resolution Isaac Newton Telescope library of empirical spectra. *Monthly Notices of the Royal Astronomical Society*, 371(2), 703-718. doi: 10.1111/j.1365-2966.2006.10699.x
- Scarlata, C., Carollo, C. M., Lilly, S., Sargent, M. T., Feldmann, R., Kampeczyk, P., . . . Takahashi, M. (2007, Sep). COSMOS Morphological Classification with the Zurich Estimator of Structural Types (ZEST) and the Evolution Since  $z = 1$  of the Luminosity Function of Early, Disk, and Irregular Galaxies. *The Astrophysical Journal Supplement Series*, 172(1), 406-433. doi: 10.1086/516582
- Schade, D., Lilly, S. J., Crampton, D., Hammer, F., Le Fevre, O., & Tresse, L. (1995, Sep). Canada-France Redshift Survey: Hubble Space Telescope Imaging of High-Redshift Field Galaxies. *Astrophysical Journal Letters*, 451, L1. doi: 10.1086/309677
- Scoville, N., Aussel, H., Brusa, M., Capak, P., Carollo, C. M., Elvis, M., . . . Tyson, N. D. (2007, Sep). The Cosmic Evolution Survey (COSMOS): Overview. *The Astrophysical Journal Supplement Series*, 172(1), 1-8. doi: 10.1086/516585
- Sérsic, J. L. (1963). Influence of the atmospheric and instrumental dispersion on the brightness distribution in a galaxy. *Boletín de la Asociación Argentina de Astronomía La Plata Argentina*, 6, 41.
- Shapley, H., & Curtis, H. D. (1921, may). The Scale of the Universe. *Bulletin of the National Research Council, Vol. 2, Part 3, No. 11, p. 171-217*, 2, 171-217.
- Simard, L. (1998, Jan). GIM2D: an IRAF package for the Quantitative Morphology Analysis of Distant Galaxies. In R. Albrecht, R. N. Hook, & H. A. Bushouse (Eds.), *Astronomical data analysis software and systems vii* (Vol. 145, p. 108).
- Swinbank, A. M., Harrison, C. M., Trayford, J., Schaller, M., Smail, I., Schaye, J., . . . Stott, J. P. (2017, May). Angular momentum evolution of galaxies over the past 10 Gyr: a MUSE and KMOS dynamical survey of 400 star-forming galaxies from  $z = 0.3$  to 1.7. *Monthly Notices of the Royal Astronomical Society*, 467(3), 3140-3159. doi: 10.1093/mnras/stx201
- Tremonti, C. A., Heckman, T. M., Kauffmann, G., Brinchmann, J., Charlot, S., White, S. D. M., . . . Brinkmann, J. (2004, Oct). The Origin of the Mass-Metallicity Relation: Insights from 53,000 Star-forming Galaxies in the Sloan Digital Sky Survey. *The Astrophysical Journal*, 613(2), 898-913. doi: 10.1086/423264
- Trimble, V. (1995, Dec). The 1920 Shapley-Curtis Discussion: Background, Issues, and Aftermath. *Publications of the Astronomical Society of the Pacific*, 107, 1133. doi: 10.1086/133671

Vogt, N. P., Forbes, D. A., Phillips, A. C., Gronwall, C., Faber, S. M., Illingworth, G. D., & Koo, D. C. (1996, Jul). Optical Rotation Curves of Distant Field Galaxies: Keck Results at Redshifts to  $z$  approximately 1. *Astrophysical Journal Letters*, 465, L15. doi: 10.1086/310136

Zwicky, F. (1933). Die Rotverschiebung von extragalaktischen Nebeln. *Helvetica Physica Acta*, 6, 110-127.

Zwicky, F. (1937, October). On the Masses of Nebulae and of Clusters of Nebulae. *Astrophysical Journal*, 86, 217. doi: 10.1086/143864



## A Details about morphological classification

We provide in this section a summary of the morphological parameters used by Cassata, Tasca and Zurich for their morphological classification which we used and compared in the present work.

### A.1 Non-parametric values

Usual galaxy classification methods rely on the same parameters. Some may use all of them when others only concentrate on a few. We give here a description of the main parameters used for this kind of classification.

#### A.1.1 Concentration

The first parameter is the concentration. Two quite different definitions exist, the former using flux levels and the latter isophotes. The oldest definition of the concentration comes from Kent (1985). In his paper, he describes it as the log of the ratio between the radii enclosing 80% and 20% of the "total" luminosity (respectively  $r_{80}$  and  $r_{20}$ )

$$C = 5 \log \frac{r_{80}}{r_{20}} \quad (21)$$

The concentration parameter can vary in theory from 1 to infinity. The parameter  $C$  as defined in Eq. 21 should be interpreted cautiously as many definitions of the "total" luminosity (sometimes also called total flux) are used. Some authors who have performed a morphological modelling might call total luminosity the integrated flux up to infinity of their best fit model. Others might use the flux within some fixed aperture (generally a multiplicative factor of the Petrosian radius  $r_p$ ), such as  $2r_p$  in Bershady et al. (2000), or  $1.5r_p$  in Lotz et al. (2004).

Another definition comes from Abraham et al. (1994). In this case, second order moments of the image are computed in order to find an outer elliptical aperture with an area similar to that of the galaxy up to some isophotal limit (generally  $2\sigma$ ). From this ellipse, the semi-major axis can be obtained. A second semi-major axis 30% smaller is derived and an inner ellipse with the same shape is defined. The concentration parameter is then computed as the ratio between the flux within the outer and the inner apertures

$$C = \frac{\sum_{(x,y) \in \mathcal{E}_{\text{in}}} I(x,y)}{\sum_{(x,y) \in \mathcal{E}_{\text{out}}} I(x,y)} \quad (22)$$

where  $\mathcal{E}_{\text{in}}$  and  $\mathcal{E}_{\text{out}}$  are respectively the inner and outer ellipses. This definition therefore yields a concentration parameter  $C$  between 0 and 1.

### A.1.2 Asymmetry

The asymmetry parameter defines how symmetric/asymmetric a galaxy is. A related parameter was first introduced by Schade et al. (1995) in order to classify galaxies as being symmetric or not, though its definition differed by using a combination of original and residual maps in its computation.

The most common definition of the asymmetry  $A$  comes from Abraham et al. (1996). The map is rotated by  $180^\circ$  and is subtracted to the original map. The asymmetry parameter is then computed as half the ratio between the total integrated intensity amplitude in the self-subtracted map and the total intensity amplitude in the original map. Using an absolute value will add a positive term in  $A$  from background signal. To get rid of it, the same calculation is performed for an aperture of the same size with only background signal and this value is subtracted from the previous one, i.e.

$$A = \frac{\sum_{i,j} |I(i,j) - I_{180}(i,j)|}{2 \sum_{i,j} |I(i,j)|} - B_{180} \quad (23)$$

where  $I_{180}$  designates the rotated map and  $B_{180}$  is the average asymmetry of the background. This definition, though commonly used, is sometimes replaced by a similar one where square brackets are used instead of absolute values. This is for instance the case in Conselice (1997). Nevertheless, both definitions yield values of  $A$  between 0 (completely symmetrical) and 1 (completely asymmetrical).

The value of  $A$  can be quite sensitive to the choice of the centre. Methods for finding the best centre position include using the brightest point in a smoothed map or iterating over  $X$  and  $Y$  till  $A$  is minimised.

### A.1.3 Gini coefficient

## B PSF FWHM variation with wavelength and MUSE field

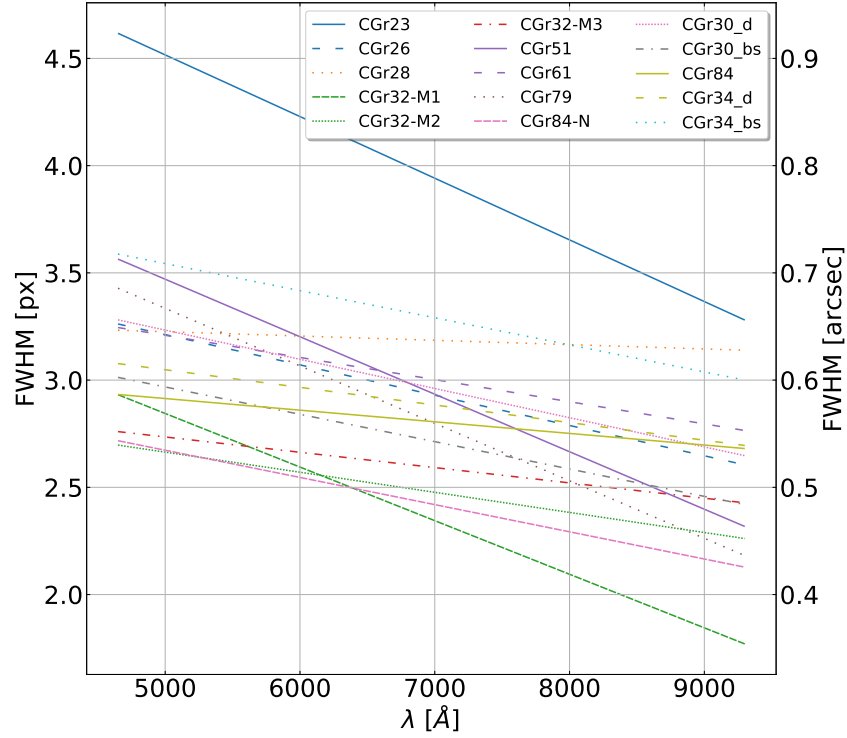


Figure 11: PSF FWHM variation with wavelength for the 13 FoVs as measured by Valentina. At least two values of the FWHM were derived from stars in the MUSE fields by fitting a Gaussian profile onto their light profile. We assumed a linear evolution with wavelength. Strong variations appear depending on the observed field.